Accepted Manuscript

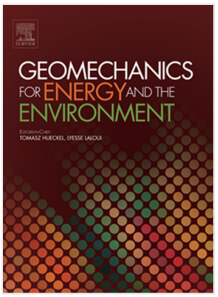

Gas migration in a cenozoic clay: Experimental results and numerical modelling

Laura Gonzalez-Blanco, Enrique Romero, Cristina Jommi, Xiangling Li, Xavier Sillen

PII: S2352-3808(16)30026-0
DOI: http://dx.doi.org/10.1016/j.gete.2016.04.002
Reference: GETE 35

To appear in: *Geomechanics for Energy and the Environment*

Received date: 10 November 2015
Revised date: 6 April 2016
Accepted date: 18 April 2016

Please cite this article as: Gonzalez-Blanco L, Romero E, Jommi C, Li X, Sillen X. Gas migration in a cenozoic clay: Experimental results and numerical modelling. *Geomechanics for Energy and the Environment* (2016), http://dx.doi.org/10.1016/j.gete.2016.04.002

GAS MIGRATION IN A CENOZOIC CLAY: EXPERIMENTAL RESULTS AND NUMERICAL MODELLING

Laura Gonzalez-Blanco[1], Enrique Romero[1*], Cristina Jommi[2], Xiangling Li[3] and Xavier Sillen[4]

Affiliation:

[1] Division of Geotechnical Engineering and Geosciences, Department of Civil and Environmental Engineering, Universitat Politècnica de Catalunya, c/ Jordi Girona 1-3, Campus Nord UPC, Edificio D-2, 08014 Barcelona, Spain, e-mail: laura.gonzalez.blanco@upc.edu; enrique.romero-morales@upc.edu

[2] Department of Geoscience and Engineering, Faculty of Civil Engineering and Geosciences, Delft University of Technology, Stevinweg 1, 2628 CN Delft, The Netherlands, e-mail: c.jommi@tudelft.nl

[3] EIG EURIDICE, European Underground Research Infrastructure for Disposal of nuclear waste In Clay Environment, Boeretang 200, 2400 Mol, Belgium, e-mail: xli@euridice.be

[4] ONDRAF/NIRAS, Belgian Agency for Radioactive Waste and Enriched Fissile Materials, Avenue des Arts 14, 1210 Brussels, Belgium, e-mail: x.sillen@nirond.be

***Contact details:**

Prof. Enrique Romero
Departamento de Ingeniería Civil y Ambiental,
c/ Jordi Girona 1-3, Campus Nord, Edificio D-2
Universitat Politècnica de Catalunya,
08034 - Barcelona – Spain, fax: +34-93 4017251
e-mail: enrique.romero-morales@upc.edu

Number of words in the main text: 6200
Number of tables: 5
Number of illustrations: 22

Abstract

Gas migration through a potential host clay formation for the geological disposal of radioactive waste in Belgium is experimentally investigated in the laboratory, and numerical modelling is performed to help in the interpretation of the results. Selected air injection tests under oedometer conditions on initially saturated Boom Clay samples with oriented bedding planes are presented in the paper. Priority in the experimental programme was given to the study of the deformation response along the injection and dissipation stages, as well as to the analysis of the pore network changes, which detect the opening of fissures that can act as preferential air pathways. The experimental results were simulated using a fully coupled hydro-mechanical finite element code, which incorporates an embedded fracture permeability model to account for the simulation of the gas flow along preferential pathways. Clay intrinsic permeability and its retention curve were assumed to be dependent on strains through fracture aperture changes. The numerical results could reproduce upstream / downstream pressures, outflow volume and soil volume change accurately. The experimental results, combined with the numerical simulation, provide good insight into the role of the volumetric response and of the bedding planes on the air transport properties of Boom Clay samples, confirming that fracture aperture occurs during gas injection, which eventually dominates further injection and pressure release stages.

Keywords: gas generation and transport, deep clay, coupled hydro-mechanical response, microstructure analysis, opening of discontinuities, preferential air flow.

1. Introduction

Most of the research work performed on the Thermo-Hydro-Mechanical (THM) behaviour of engineered barriers concerns the initial transient hydration processes under the combined action of the water infiltrating from the host rock and the heat generated by the canister. The experimental information concerning this transient process covers only a short time period of the expected lifetime of the barrier.

The long-term behaviour of clay barriers has received comparatively less attention. A significant issue in the long-term performance of clay buffers and the surrounding host rock concerns the generation and migration of gases. Actually, in the post-closure phase of a disposal system, gases can be produced as a result of the anaerobic corrosion of metal canisters, radiolysis, microbial degradation of organic waste and radioactive decay [1]. The pressure resulting from the gas generation in an almost impermeable geological medium in the near-field of a repository will increase. Under high gas pressures, the mechanical and hydraulic properties of the host rock and the barrier system are expected to change significantly, which eventually may lead to the release of the produced gases.

Belgium has been studying during the last decades the Boom Clay as a potential deep and sedimentary clayey formation for the geological disposal of long-living and heat-emitting radioactive waste. Research efforts have been spent on understanding gas migration in sedimentary rocks [2, 3, 4, 5], and several laboratory and in-situ studies have been performed on gas transport in engineering barrier systems. Within the FORGE project [4, 5], consensus grew on the hypothesis that in such low permeability porous media, saturated with water or close to saturation, transport of free gas occurs by the creation of specific gas pathways, which, in turn, trigger further creation or reactivation of discontinuities in the porous medium.

Marschall et al. [6] suggested different basic transport mechanisms depending on the gas generation rate, based on purely phenomenological considerations. In a saturated medium, the dominant process is diffusion and advection of dissolved gas for low gas generation rate. A separate gas phase may develop at increasing gas generation rate, and two-phase flow will occur if the gas pressure is higher than the gas entry pressure. At high gas generation rate, the gas pressure may increase significantly. At constant

93 confining stress, increase in gas pressure starts affecting the mechanical response of the
94 rock: unloading will be responsible of expansion of the clay, and eventually of its
95 degradation, which in turn will affect the gas migration. Micro-fissures can be generated
96 as a result of the high gas pressures and the relatively low tensile strength of the clay
97 rock. This micro-crack network can provide additional pathways for the gas flow.

98 In spite of the interest for long term prediction of waste disposal barriers performance in
99 sedimentary rocks, careful investigation of the coupled hydro-mechanical response of
100 sedimentary formations in relation with gas migration has not received much attention,
101 until recently [7, 8, 9, 10]. The latter studies showed that migration of gas in low
102 permeability rock formations is a rather complex phenomenon, governed by different
103 coupled mechanical and hydraulic processes. Specifically, intrinsic permeability,
104 porosity and water saturation, stress state and stress history, shear strength, strain level
105 and damage are all playing a role in the response, as well as the gas generation rate and
106 the gas pressure in the near field. Therefore, coupled hydro-mechanical experimental
107 tests are mandatory, in which gas migration is investigated to adequately evaluate the
108 long-term safety of the disposal system.

109 Experimental data on Boom Clay are still poor, with the exception of the results from
110 laboratory tests within the framework of the MEGAS project [11] and recent gas
111 diffusion experiments [12, 13]. To improve the knowledge on Boom Clay response to
112 gas migration and the predictive capabilities on the long term behaviour of Boom Clay
113 as host formation, a comprehensive series of air injection tests under oedometer
114 conditions is being performed at the Universitat Politècnica de Catalunya. Relatively
115 fast volume rate air injections tests (air pulse tests) have been performed to give priority
116 to dominant single-phase air flow mechanisms associated with the opening of stress-
117 dependent discontinuities, rather than on slower two-phase flow and air diffusion
118 mechanisms through the matrix. The tests are designed specifically on samples with
119 oriented bedding planes to investigate their effects on the coupled hydro-mechanical
120 mechanisms dominating gas migration, pressurisation and release in the clay. Contrarily
121 to previous works [2, 12, 13, 14, 15], volume changes are allowed in the experimental
122 setup, and the deformation response is analysed during air injection, air pressure
123 increase and dissipation.

Particular attention is given to the change in the pore network in order to detect the opening of fissures or discontinuities due to the air migration, by analysing the pore size distribution (PSD) before and after the gas injection tests on data from mercury intrusion porosimetry. The PSD data are used to show the evidence of preferential pathways formed during gas injection and pressurisation and, to calibrate the hydraulic laws used in the numerical simulations of the tests.

Results of finite element numerical simulations performed with the Code_Bright [16], are compared with relevant experimental measurements. An embedded fracture permeability model [17] was used to explain the gas breakthrough observations. The embedded fracture permeability model allows tracking the degradation of the soil sample under gas pressurisation (increasing gas permeability) and helps in the comprehension of the local coupled processes dominating the response of the material.

2. Soil properties and experimental methods

2.1 Boom Clay samples

Boom Clay, which was deposited 36 to 30 million years ago during the Rupelian age (Northwest European Tertiary Basin), is located between 160 and 270 m depth at Mol (Belgium) in an almost horizontal layer with a slight 1-2% north-east dip. The samples used in this study were collected at a depth of 223 m in the URL (Underground Research Laboratory) HADES (borehole 2012/2 in the Connecting Gallery, Ring 70-71 -horizontal borehole towards the west-). The main mineralogical composition of the Boom Clay is: 20-30% kaolinite, 20-30% illite, 10-20% smectite, 25% quartz and feldspar. Table 1 summarises the main properties of this clay and includes the initial test conditions, which replicate the *in situ* conditions. Saturated Boom Clay specimens displayed high initial suction due to stress relief upon sampling. The total suction measured in the laboratory was 2.5 MPa, in good agreement with the data reported in [18, 19, 20]. Water retention data on drying are plotted in Figure 1, which allows estimating an air-entry value of about 5 MPa (higher than the initial suction) for an initial void ratio 0.61. The data were obtained using a dew point psychrometer, by stepwise drying of the specimens starting from the initial suction. The data are fitted to the van Genuchten's equation indicated in the figure.

To characterise the initial pore network, mercury intrusion porosimeter (MIP) tests were performed [21]. Figure 2 presents the pore size density function – calculated based on the intruded volume of mercury referred to volume of solids (non-wetting void ratio e_{nw}) –, which showed a mono-modal distribution with a dominant entrance pore size of 70 nm (Figure 2). This dominant pore size is associated with an air-entry value of 4.8 MPa (Table 1).

2.2 Experimental equipment and protocol

A high pressure oedometer cell [20] was chosen to perform the air injection tests, because of its high stiffness and the simplicity in measuring sample volume changes. The soil samples, 20 mm thick and 50 mm in diameter, were placed between the top and bottom caps made of concentric stainless steel rings, which operate as coarse porous stones allowing the injection and recovery of water and air. A hydraulic vertical piston with a maximum capacity of 10 MPa was used to apply the vertical stress. Vertical displacements were measured with an external LVDT. The experimental setup includes four automatic pressure/volume controllers: besides the one for the vertical stress, one was adopted for air injection (upstream boundary - bottom of the sample -) and two for water (injection at upstream and recovery at downstream boundaries). The cell and auxiliary devices are presented in Figure 3.

The oedometer tests were run with the protocol described below and depicted in Figure 4.

1. Pre-conditioning path. The main objective of this initial path was to restore the *in situ* effective vertical stress after pore water pressure equalisation [22]. The pre-conditioning path consisted into two stages:

a) water undrained loading stage up to σ_v = 3 MPa at a rate of 15 kPa/min at constant water content and atmospheric air pressure p_a = 0;

b) contact with synthetic Boom Clay water (SBCW) at atmospheric pressure p_w=0 (synthetic water was prepared according to [23]).

2. Hydraulic conductivity of the intact samples was determined at steady-state under a pressure gradient of 0.1 MPa (upstream and downstream water pressures were 0.6 and 0.5 MPa, respectively) and at constant total vertical stress (σ_v = 3 MPa).

3. Loading stage at controlled stress rate 0.5 kPa/min to ensure drained conditions, to a total vertical stress σ_v = 6 MPa at constant water pressure (0.5 MPa). This maximum effective vertical stress (5.5 MPa) did not exceed the yield stress of the clay (around 5.6 MPa), as will be later shown. At the same time, σ_v is large enough to inject air at a pressure up to 4 MPa and avoid passage of air between sample and oedometer ring (coefficient of lateral earth pressure at rest K_0= 0.84, [24]).

4. A fast drainage of the bottom line was performed at σ_v = 6 MPa to replace water by air. An initial air pressure of 0.5 MPa was applied at the upstream boundary.

5. Air injection at constant controlled volume-rate to a maximum of 4 MPa (bottom cap). At this air pressure, the injection piston was stopped (shut-off) and air pressure was let to decay at constant air volume of the inlet line. This maximum air pressure was limited to 4 MPa to avoid exceeding the minor principal stress (radial stress σ_h in the figure) and the air-entry value of the material (refer to Table 1). Tests at two different injection rates were performed (namely 2 mL/min and 100 mL/min) to observe its influence on the coupled hydro-mechanical response. The selected rates were however relatively fast (air pulse tests), in order to minimise air diffusion mechanisms through the matrix and to enhance single-phase air flow mechanisms through discontinuities. During the air injection stage, the downstream lines were full of water and the controller was kept at constant pressure of 0.5 MPa. This controlled downstream pressure increased when the air outflow was high, since the pressure/volume controller was not able to keep this constant pressure condition (a maximum pressure of 1.8 MPa was prescribed by a pressure release valve).

6. Final unloading stage under undrained conditions.

After each injection test a MIP test was performed to study the changes in the pore size distribution of the clay. Moreover, complementary reference oedometer tests were performed, following the same stress paths but avoiding the air injection stage, so that

changes in the pore size distribution could be uniquely related to air injection and transport.

2.3 Compressibility and water permeability

Figure 5 shows continuous loading results at controlled stress rate in terms of axial strain (positive in compression) as a function of the vertical stress in the reference oedometer tests, where the SBCW was placed in contact with the sample at a vertical stress (3 MPa) approximately equivalent to the *in situ* effective stress. These reference tests were carried out independently from the air injection tests, and included a drained unloading path after attaining $\sigma_v = 6$ MPa. The as-retrieved samples showed high stiffness at the beginning, due to the high initial suction, while the stiffness decreased after contact with the SBCW. In order to evaluate the slope of the virgin compression curve, some of the tests were brought to stresses higher than the estimated yield stress, which is around 5.6 MPa.

The water permeability was determined at several loading stages of the oedometer tests, at different stress states and pressure gradients in order to establish a correlation with the porosity of the clay. Figure 6 presents the relation between water permeability and average void ratio. The results refer to samples in which the direction of the flow was parallel to the natural bedding planes, of interest for this investigation, and they are in good agreement with results reported by other authors [25].

3. Tests results

3.1 Air injection tests

Selected results of the air injection and dissipation stages at constant vertical stress are presented in Figure 7. The figure shows the time evolution of the air injection pressure at the upstream boundary and the outflow pressure and volume at the downstream boundary, jointly with the average axial strain, calculated based on recorded axial displacement. The tests were performed on two samples with bedding planes parallel to air flow, at different injection rates, 100 mL/min and 2 mL/min. The time evolutions of the relevant variables display similar pattern. The air pressure at the upstream boundary increased in time from 0.5 to 4 MPa (*A* to *B* in the figure), followed by shut-off (point

B) and dissipation at closed air injection line (*B* to *C*). The outflow volume rapidly increased indicating the break-through time until the downstream controller was filled (refer to the faster air injection test). At this break-through time the outflow pressure started to increase until the maximum of 1.8 MPa limited by a release valve was reached. Increase in injection pressure was accompanied by expansion (negative axial strains), followed by compression strains along the dissipation stage. The first air outflow break-through depended on the injection rate. In samples tested at 100 mL/min, the first outflow was detected during the dissipation stage, whereas in samples tested at 2 mL/min it already occurred during the last phase of the injection stage.

Figure 8 presents the evolution of the average axial strain with a measure of the net stress at the bottom boundary, defined as the vertical stress, σ_v, minus the air pressure at the bottom injection boundary, p_a. The net stress at the bottom boundary, $\sigma_v - p_a^{bottom}$, is used as a "constitutive stress variable" to provide an initial interpretation of the deformation response of the material. Data during the air injection and dissipation stages of the two selected tests at two volume-injection rates are presented. The samples, kept at constant vertical stress (6 MPa) displayed some expansion during the early air injection stage (*A* to *B* in Figure 8), which was slightly larger at the slower air injection rate. After shut-off (point B in the figure), expansion continued in the sample subjected to faster air injection (*B* to *B'* in the figure) as the air pressure front propagated into the sample, inducing the fluid pressure to increase and the constitutive stress to decrease. After shut-off, no expansion was observed on the sample subjected to the slower air injection rate, since the pore pressure was nearly equilibrated during air injection. Some elapsed time later after shut-off, the air injection pressure started to decline along the dissipation stage towards point *C*. Consequently, the constitutive stress increased inducing compression on the material. The sample subjected to the slower injection rate showed a quasi-reversible volume change response along the dissipation stage.

Figure 9 shows a comparison of the stiffness of the soil samples during air injection with the stiffness from data of conventional drained unloading paths (refer to Figure 5). For the latter, the drained constrained modulus is estimated as the ratio between the change in effective stress of samples saturated with water and the corresponding changes in axial strain, $E'_k = \delta(\sigma_v - p_w)/\delta\varepsilon_a$. These unloading results reveal that on

saturated Boom Clay the drained constrained modulus drops considerably due to swelling of the sample in contact with water during the drained unloading path. The air injection stage, considered equivalent to an unloading stage of the material, was also analysed in terms of stiffness $E'_k = \delta(\sigma_v - p_a^{bottom})/\delta\varepsilon_a$. At the beginning of the unloading stage, the constrained modulus was similar to the saturated samples, but during the air injection process Boom Clay displayed a higher stiffness (Figure 9).

3.2 Pore size distribution changes after air tests

The previous results suggested that some changes in the pore size distribution of the samples could take place during injection. To better investigate the consequences of air injection, MIP tests were performed on freeze-dried samples to compare the pore network before (intact state) and after the air tests. Figure 10 presents the pore size density functions obtained for the intact material and after the air tests. Special care was taken during the unloading stage under undrained conditions (after the air tests) to prevent further expansion of the material. As indicated in the figure, a new family of large pores, which was not detected on intact samples, was observed after the tests. This new dominant pore size at entrance sizes larger than 2 μm appeared to be associated with the expansion undergone by the material during the air injection stage. Figure 10 also includes the pore size distribution of a sample after loading and fast undrained unloading, which therefore followed the same loading path, but without the injection stage. The large pores were not detected on this sample, which suggested that they were actually related to the air injection / migration process. Two types of pore domains were thus considered: a) small pores (micropores) associated with the clayey matrix and with dominant pore size around 70 nm, and b) large pores (macropores) related to the opening of fissures and with entrance sizes larger than 2 μm.

To better understand the nature of these pore domains, MIP data were interpreted in terms of the fractal character of the porous network, admitting self-similarity of the hierarchical void structure [21]. Figure 11 shows the fractal dimension D_s of the porous medium, obtained from the change of the intruded pore volume (non-wetting degree of saturation, S_{rnw}, of intruded mercury referred to total pore volume) with respect to the change in mercury intrusion pressure, p. The fractal analysis on intact material indicates a pore domain for sizes < 100 nm with $D_s \approx 2$ and a larger size domain (typically higher

than 1 μm) with $D_s \approx 3$. The same pattern was found in the sample tested without the air injection stage. Nonetheless, the fractal analysis on samples tested after the injection tests indicates a decrease of the fractal dimension $D_s \approx 2.5$ of the new family of large pores developed. It appears that this macroporosity tends to a fissure-like structure, consistent with the opening of fissures during the expansion undergone by the material along the air injection stage. The visual observation after dismantling the tested samples showed some areas drier than others in the same direction as bedding orientation. This fact indicated the desaturation due to air passage through these fissures following the bedding planes.

4. Numerical simulation of selected results

To provide further insight into the air injection process and on the consequences on the deformation response, a numerical analysis was performed.

4.1 Background information

In most cases, the models used to simulate gas migration processes are based on the concept of two-phase flow through continuous porous media. Stress-dependent porosity and permeability are often used as a way to better reproduce rapid increase of gas flow above a threshold injection pressure [10]. Other approaches suggest to couple explicitly two-phase flow transport models with poro-mechanics models [26, 27] to better take into account the role of the evolving stress field. The latter models are claimed to better reproduce the effect of pathway dilation on gas transport at the relevant scale of the system. The Two-Part Hooke's Model (TPHM) has been used as a possible alternative, which assumes that sedimentary rocks can be thought as a superposition of 'soft' and 'hard' parts [28, 29]. The model applied to a layered structure is conceived with soft layers undergoing relatively large strains, thus showing higher permeability, and hard layers which undergo small strains [30]. To take into account material anisotropy and the possible presence of preferential gas transport pathways along a given orientation, other authors used embedded fracture permeability models or added joint elements to a continuum model [14, 31]. In many cases, the experimental data could be reproduced reasonably well by the previous approaches for what concerns gas pressure evolution. On the contrary, the deformational behaviour during the gas transport process has been seldom tackled.

In this work an embedded fracture model in a fully coupled hydro-mechanical approach was adopted to simulate the gas injection tests. The coupled solution of the mechanical and two-phase flow equations is performed using finite elements with Code_Bright [16]. The adopted approach for gas and water flow through discontinuities including mechanical interactions was described and demonstrated on some synthetic cases in [32] and in [17], and afterwards applied to some experimental results on sand/bentonite [15] and claystone [14].

Actually, modelling this type of tests is a challenging task and involves several aspects. The main objective of the tests simulations is to better understand the coupled hydro-mechanical consequences of gas flow passage through the material by analysing the deformational response recorded in the experimental tests.

A 2D axisymmetric representation of the sample was selected. Both for the constitutive model and the geometry of the problem simple approximations, still able to capture the consequences of preferential path development, were made. The sample was modelled by two zones having different hydraulic properties: the matrix and the zone of fracture development (ZFD) in which the dominant advective flow of gas occurs. In the choice of the latter, a single predefined central zone was chosen, renouncing to investigate the local distribution of the fractures, but still keeping the possibility of reproducing the global effect of the localised preferential paths on the sample response. For the matrix and the embedded fracture zone the same mechanical parameters were chosen, but different hydraulic models were used. Soil volume changes will be analysed.

4.2 Constitutive laws

The mechanical model adopted for the Boom Clay is the elastoplastic model BBM (Barcelona Basic Model, [33]). To model the effects of the localised fissures along the bedding planes (gas pathways parallel to bedding planes), a fracture development zone is added, where the embedded fracture permeability model is applied. This hydraulic model can take into account the variation of the intrinsic permeability and the capillary air entry pressure with fracture aperture, which depends on strain.

The intrinsic permeability of the matrix depends on the porosity ϕ through Kozeny's law

$$k_{matrix}(\phi) = k_0 \frac{\phi^3}{(1-\phi)^2} \frac{(1-\phi_0)^2}{\phi_0^3} \quad (1)$$

where k_0 is the intrinsic permeability for the reference porosity ϕ_0.

In the single fracture, liquid and gas flow are computed using Darcy´s law, with the intrinsic permeability calculated assuming laminar flow, as

$$k_{fracture} = \frac{b^2}{12} \quad (2)$$

where b is the fracture aperture.

The equivalent element permeability is computed as follows

$$k_{element} = k_{matrix} + \frac{b^3}{12s} \quad (3)$$

where s is a characteristic dimension for a specific rock. This parameter, which weights the role of the fractures on the hydraulic response, governs the constitutive functions for permeability and capillary pressure variations. Therefore, it was chosen as fitting parameter based on the available experimental data from water retention curve and intrinsic permeability values.

The current aperture b can be estimated as a function of the strain ε (positive when describing expansion in the model) from

$$b = b_0 + \Delta b \quad \text{for} \quad \Delta b \geq 0 \quad (4)$$

$$\Delta b = s\Delta\varepsilon = s(\varepsilon - \varepsilon_0) \quad \text{for} \quad \varepsilon > \varepsilon_0 \quad (5)$$

Therefore the local strain results in changes in aperture. The strain perpendicular to the fracture plane was chosen to estimate the aperture change. The threshold strain ε_0 is associated with fracture initiation. In this study, an existing fracture is considered with an initial aperture b_0, and is assumed to be initially open at $\varepsilon = 0$ (i.e., $\varepsilon_0 < 0$ and $b = b_0 + s(-\varepsilon_0) > b_0$). Normal extension will induce further aperture opening ($\varepsilon > \varepsilon_0$). Unloading will imply fracture closure, but a residual aperture is expected owing to irreversible strains.

The variation of capillary air entry pressure caused by changes in the aperture is also included. The capillary air entry pressure, P, necessary to desaturate a fracture is given by

$$P = \frac{2\sigma \cos\theta}{b} \tag{6}$$

where σ is the surface tension and θ the contact angle.

This equation can be used directly to calculate the air entry value of the element. If Eq. (6) is combined with Eq. (2), then the capillary air entry pressure to start desaturation is obtained as

$$P = P_0 \sqrt[3]{\frac{k_o}{k}} \tag{7}$$

where $P_0$is the capillary pressure for a reference permeability k_0, which eventually can be the initial permeability.

Additional details of the embedded fracture permeability model are given in [17]. The hydraulic equations used in the simulations are listed in detail in the Appendix.

4.3 Model parameters

Table 2 lists the mechanical parameters required for the BBM model used in the present calculations and determined from different hydro-mechanical tests performed during this study. This set of parameters is in accordance with those reported in [25] for Boom Clay. Figure 12 shows the results of the numerical simulation of one of the mechanical compression paths in Figure 5. The model is capable of reproducing the initial loading, the swelling upon contact of the sample with the SBCW and the drained loading very well.

For the retention properties of the matrix material the van Genuchten's model is adopted, while a power law is considered for both liquid and gas relative permeability fitting the experimental data reported by [11]. Table 3 shows the hydraulic constitutive parameters considered in the analysis. The diffusion coefficient was selected according to [13] for samples with bedding planes parallel to the flow direction. In Figure 13 the fitted Kozeny's model for the intrinsic permeability changes of the matrix as a function

of void ratio is shown, together with the experimental measurements for samples with bedding planes parallel to water flow.

The required parameters for the embedded fracture permeability model were fitted by using experimental data. An initial aperture $b_0 = 100$ nm – slightly higher than the dominant pore mode of the matrix – was selected (Figure 2). The threshold strain, ε_0, and the characteristic dimension, *s*, were fitted so as to achieve a final capillary pressure in the ZFD similar to the one determined by MIP after the air injection tests. The procedure to obtain the water retention curve from MIP data is described in [21]. The theoretical variation of the intrinsic permeability and the capillary pressure with the selected parameters – according to Eq. (2) and Eq. (7) – is depicted in Figure 14 together with the corresponding initial and final values. The initial and the final water retention curves of the ZFD – obtained with the initial and final value of the capillary pressures, respectively – are in good agreement with the experimental data (Figure 15).

4.4 Boundary conditions at the injection stage

To properly simulate the test, it is necessary to include both the injection and recovery systems in the model, which correspond to the drainage lines of the experimental set-up. If these were not explicitly included in the numerical model, the actual injection and outflow pressures history at the boundaries of the sample would not be properly assigned, because the change in the density of the pressurised mass of air would be disregarded. After the shut-off the mass of pressurised air in the upstream injection system is significant and cannot be disregarded. Accounting for the controlling system flexibility was achieved by adding to the model two reservoirs, which represent the injection and recovery pistons, lines and coarse porous rings. These elements are idealised with a porosity of 0.5 (the code cannot simulate non-porous materials), high conductivity (permeability of 10^{-10} m^2) and a flat retention curve with a very low air entry value ($P_0 = 0.001$ MPa). The total volume of each system corresponds to the volumes obtained from calibration tests of the equipment. The mechanical constitutive law for these stiff elements was linear elasticity with a very high Young modulus. The final geometry of the discretised problem is depicted in Figure 16. Null vertical displacements at the bottom of the system and null radial displacement on the sample lateral wall are imposed to simulate oedometer conditions.

Before the air injection starts, the sample is fully saturated, as well as both reservoirs. The first stage of the injection consists in replacing the water in the upstream reservoir by air at 0.5 MPa pressure. An injection pressure ramp is then applied at the bottom of the injection reservoir, which follows the recorded data during the test. The dissipation stage starts once the injection pressure reached the maximum pressure of 4 MPa. The bottom boundary becomes impermeable along this dissipation stage forcing the accumulated air in the reservoir to flow upwards.

The pressure of the downstream pressure/volume controller is kept constant at 0.5 MPa during the tests. This device is capable of maintaining this pressure by changing the volume as the air flows through the sample. However, when the tank of the controller is full, it is not able to keep the pressure anymore if the air flow continues and thus the pressure begins to rise. In contrast, the upper reservoir in the simulation has a fixed volume. As a result, an increase in the outflow pressure must be imposed in the numerical model to properly model the boundary conditions. Accordingly, the pressure boundary condition in the downstream reservoir was set constant in the first stage of the simulation - water pressure at 0.5 MPa - and was increased up to 1.5 MPa in the last stage. Table 4 summarises the simulation stages for the air injection.

4.5 Simulation of slower air injection test

The results of the computed injection and outflow pressure response in the ZFD (at 0.0005 mm from the axis) as a function of time together with the outflow volume and the average axial strain along the sample height are shown in Figure 17 compared with experimental results for the sample tested at the slower injection rate.

Figure 17a shows that the air pressure decay at the bottom of the sample during the dissipation stage is acceptably well fitted. Good agreement is also found on the fluid pressure at the top, computed as the maximum between air and water pressure. The computed sample volume change represented by the average axial strain is also reasonably well reproduced (Figure 17b). The sample at an air injection rate of 2ml/min undergoes expansion during the injection stage followed by compression during air dissipation. The computed results show the same expansion, while a slightly larger compression than the measured one is predicted.

Moreover, the time in which the outflow takes place (Figure 17c) compares well with the measured one. Fixing the pressure boundary conditions at the downstream reservoir as explained above, the outflow volume, computed as the sum of water and air volumes, fits well with the experimental measurements.

The local sample response is depicted in Figure 18, with contour plots to better understand the influence of the embedded fracture response. Absolute gas pressure, porosity and liquid degree of saturation are represented at three different time steps. The first one refers to 150 minutes after the start of gas injection, the second at the end of the gas injection (shut-off) and finally during the dissipation stage. It is worth noting that the opening of the fracture plays an important role in terms of air dissipation. On the one hand, only when the air pressure increased enough, the fracture opens and becomes desaturated, allowing the air to flow. On the other hand, as the air pressure decreases due to the outflow, the fracture gradually closes up over the time. The matrix of the clay presents a significant delayed behaviour, as its permeability does not change as the same rate. Moreover, it remains fully saturated after the air passage. Indeed, within the matrix, the dominant transport mechanism is the diffusion of dissolved air. Figure 19 shows the contribution of the diffusive and advective flows in the matrix and in the ZFD at three different elapsed times. The dominant advective flow in the ZFD is clearly observed. The simulated vertical profiles in the ZFD of the gas and the liquid pressures at the same elapsed times are shown in Figure 20, where the evolution of the gas pressure front along the ZFD can be clearly appreciated.

In Figure 21 the computed local radial strains (positive in compression) show that the oedometer constraint does not prevent local radial strains associated with the aperture of the fracture. The local strains start developing at the beginning of the gas injection and clearly reach their maximum in correspondence of the maximum aperture of the fracture. The intact matrix is subjected to compressive strains which compensate the extension strains of the ZFD. Afterwards, they decrease during the dissipation stage. It is worth noting that the non-null radial strain at the boundary of the sample is a numerical artefact due to calculation of strains at the Gauss points. The position of the maximum radial displacement moves towards the external boundary during the injection tests, and its value at the boundary is correctly null, as shown in the same figure.

4.6 Prediction: faster air injection test

The parameters of the embedded fracture model were calibrated by comparison with the slower injection test. To demonstrate the predictive capability of the numerical model, the air injection test at 100 mL/min was simulated with the previous set of parameters, representing a blind test. The stages of the simulation were changed to adapt them to the faster injection as the injection stage lasted only 4.87 minutes, but keeping the same criteria regarding boundary conditions as before (Table 5).

Figure 22 presents the computed results together with the experimental ones showing a general good agreement. The pressure release in the simulation was slower than the measured, and thus the average expansion axial strain is slightly higher. However, the overall deformation behaviour is well captured, displaying some expansion at the early injection stage which continues after the shut-off, while the air pressure front propagates into the sample. Afterwards, during the air pressure dissipation stage, progressive compression of the sample is well caught. The outflow volume breakthrough at the top of the sample is well reproduced, although the amount of outflow is slightly overestimated.

5. Concluding remarks

Experimental data are essential to provide deeper understanding of the long-term consequences of gas flow through saturated clays such as Boom Clay. The results presented in this paper correspond to two oedometer tests carried out with orientated bedding planes -parallel to air flow- and different injection rates. The main focus was given to the coupled hydro-mechanical response, tracked through the measurements of the axial displacements during the experimental tests, and complemented with results from numerical simulations allowing preferential paths development. Injection and dissipation stages were examined in order to investigate the volume change behaviour and the hydro-mechanical coupling in the gas migration process in Boom Clay, as well as to examine the consequences of preferential path development.

The air injection tests were performed in a dedicated oedometer at a constant vertical stress of 6 MPa, on samples with pre-defined orientation of bedding planes, parallel to the direction of flow. The maximum air pressure was achieved by injecting air at

537 constant volume rate. In order to not exceed the minimum stress (radial stress) and the
538 air entry value, the maximum air pressure target was 4 MPa. In the analysed tests, large
539 amounts of fluid volume were measured at the downstream reservoir which indicated
540 the break-through point was exceeded. The deformation response during the process is
541 fully coupled with the hydraulic process. The samples underwent expansion during the
542 air injection (stress decrease), and compression when the air pressure decayed (stress
543 increase). MIP tests allowed detecting a new family of large pores with entrance sizes >
544 2 μm after the gas injection tests and displaying a fractal dimension that suggests a
545 fissure-like structure.

546 The results of the experimental tests, already providing better insight into the long term
547 behaviour of the material subjected to gas injection, can be further evaluated with the
548 aid of numerical analysis, which give preliminary suggestion on the local stress-strain
549 response of the sample in oedometer. A FE coupled hydro-mechanical code was used to
550 analyse the results, adopting an embedded fracture permeability model within the
551 continuous elements of the matrix in order to simulate the fracture opening in the
552 material. The initial aperture of the fracture was set based on the dominant entrance
553 pore size detected by MIP, and the current aperture was assumed to be governed by the
554 local normal strain, once this overran a threshold strain. One of the experimental tests
555 was used to calibrate the unknown parameters, while a second one was performed as a
556 blind prediction test. It is worth noted that including the upstream and downstream
557 reservoirs explicitly is necessary to simulate the flexibility of the experimental system
558 and to accomplish reliable results, by properly assigning the conditions time history at
559 the boundaries of the sample.

560 The comparison between the experimental data and the model predictions shows
561 encouraging agreement. The simple numerical model implemented for the analysis of
562 these oedometer tests provided some interesting information on the local hydro-
563 mechanical coupled response of Boom Clay subjected to gas formation, pressurisation
564 and transport. However, realistic modelling in a more general geometric configuration
565 can be achieved only by integrating the embedded fracture model in all the elements.
566 Including random permeability (or porosity) fields, like the ones proposed by Arnedo et
567 al. [14], would allow heterogeneity to automatically develop fracture patterns, without
568 the need for a pre-defined fracture zone. The experimental and numerical studies are

569 continuing with the analysis of the influence of the inherent anisotropic structure of the
570 Boom Clay.
571

572 **Acknowledgements**

573 The authors are grateful to the Belgian agency for radioactive waste management
574 (ONDRAF/NIRAS) for their financial support. Thanks are also expressed to Prof.
575 Olivella for his valuable comments regarding the numerical modelling.
576

Appendix: Hydraulic constitutive equations

Liquid and gas flows follow Darcy's law

$$\boldsymbol{q_l} = -\boldsymbol{K_l}(\nabla P_l - \rho_l \boldsymbol{g}) \quad (8)$$

$$\boldsymbol{q_g} = -\boldsymbol{K_g}(\nabla P_g - \rho_g \boldsymbol{g}) \quad (9)$$

where P_l and P_g are liquid and gas pressures, respectively, $\rho_l = \rho_{l0}\, exp\,(\beta\,(P_l - P_{l0}))$ (β = liquid compressibility) is the liquid density, ρ_g is the gas density and $\boldsymbol{K}_\alpha = \boldsymbol{k} \cdot k_{r\alpha}/\mu_\alpha$ is the permeability tensor. The intrinsic permeability tensor, $\boldsymbol{k}$, depends on the pore structure of the porous medium. $k_{r\alpha}$ is the value of relative permeability, which controls the variation of permeability in the unsaturated regime and μ_α denotes the dynamic viscosity. In this expressions, α may stand for either l or g depending on whether liquid or gas flow is considered. The relative permeability of liquid and gaseous phases depend on degree of saturation using empirical relationships. $\boldsymbol{g}$ is the gravity vector.

The relative permeability of liquid (k_{rl}) and gaseous (k_{rg}) phases are made dependent on S_e (effective degree of saturation) according to

$$S_e = \frac{S_l - S_{lr}}{S_{ls} - S_{lr}} \leq 1 \quad (10)$$

$$k_{lr} = S_e^n \qquad \text{(generalised power law)} \quad (11)$$

$$k_{gr} = A\,(1 - S_e)^\beta \qquad \text{(generalised power law)} \quad (12)$$

where S_l is degree of saturation, S_{lr} and S_{ls} are residual and maximum degrees of saturation, respectively, and A, n and β are material parameters.

It is also necessary to define the retention curve of the materials by relating degree of saturation with suction ($s = (P_g - P_l) \geq 0$). The expression selected (van Genuchten's model) is

$$S_e = \frac{S_l - S_{lr}}{S_{ls} - S_{lr}} = \left(1 + \left(\frac{s}{P_0}\right)^{1/1-\lambda}\right)^{-\lambda} \quad (13)$$

601 where P_0 is a parameter related to the capillary pressure and λ is a parameter which
602 controls the shape of the curve. Hysteresis effects have not been taken into account in
603 the analysis.

604 Finally, molecular diffusion of dry gas in liquid is governed by Fick's law

605 $$\boldsymbol{i}_l^a = -(\tau\phi\rho_l S_l D_m^a \boldsymbol{I})\nabla\omega_l^a \qquad (14)$$

606 where $\boldsymbol{i}_l^a$ is the non-advective mass flux of gas in liquid, τ is the tortuosity, ϕ is the
607 porosity, ω_l^a is the mass fraction of gas in liquid and D_m^a is the molecular diffusion
608 coefficient of dry gas in liquid.
609

References

[1] ONDRAF/NIRAS, "Research, Development and Demonstration (RD&D) Plan for the geological disposal of high-level and/or long-lived radioactive waste including irradiated fuel of considered as waste, State-of-the-art report as of December 2012," *ONDRAF/NIRAS, report NIROND-TR 2013-12 E*, 2013.

[2] S. T. Horseman, J. F. Harrington, and P. Sellin, "Gas migration in clay barriers," *Eng. Geol.*, vol. 54, no. 1–2, pp. 139–149, 1999, doi: 10.1016/S0013-7952(99)00069-1.

[3] R. Cuss, J. Harrington, R. Giot, and C. Auvray, "Experimental observations of mechanical dilation at the onset of gas flow in Callovo-Oxfordian claystone," *Clays Nat. Eng. Barriers Radioact. Waste Confin. Geol. Soc. London, Spec. Publ.*, vol. 400, pp. 507–519, 2014, doi: 10.1144/SP400.26.

[4] R. P. Shaw (Ed), "Gas Generation and Migration," in *International Symposium and Workshop 5th to 7th February 2013 Luxembourg, Proceedings*, 2013, p. 269.

[5] J. Harrington, G. Volckaert, E. Jacobs, N. Maes, L. Areias, R. Charlier, C. Frédéric, P. Gerard, J. P. Radu, J. Svoboda, S. Granet, J. Alcoverro, D. Arnedo, S. Olivella, E. Alonso, P. Marschall, I. Gaus, J. Rüedi, R. Cuss, S. Sathar, and D. Noy, "Summary report : Experiments and modelling of excavation damage zone (EDZ) behaviour in argillaceous and crystalline rocks (Work Package 4)," *EC FORGE Proj. Rep. D4.24-R*, 2013.

[6] P. Marschall, S. Horseman, and T. Gimmi, "Characterisation of Gas Transport Properties of the Opalinus Clay, a Potential Host Rock Formation for Radioactive Waste Disposal," *Oil Gas Sci. Technol.*, vol. 60, no. 1, pp. 121–139, 2005, doi: 10.2516/ogst:2005008.

[7] E. Romero, R. Senger, P. Marschall, and R. Gómez, "Air tests on low-permeability claystone formations. Experimental techniques, results and simulations," in *International Workshop Advances in Multiphysical Testing of Soils and Shales*, 2012, pp. 69–83, doi: 10.1007/978-3-642-32492-5_6.

[8] E. Romero and R. Gómez, "Water and air permeability tests on deep core samples from Schlattingen SLA-1 borehore," *NAGRA Rep. NAB 13-51*, 2013.

[9] E. Romero and L. Gonzalez-Blanco, "Complementary water and air permeability tests on core samples from Schlattingen SLA-1 borehole," *NAGRA Rep. NAB 15-06*, 2015.

[10] R. Senger, E. Romero, A. Ferrari, and P. Marschall, "Characterization of gas flow through low-permeability claystone: laboratory experiments and two-phase flow analyses," *Geol. Soc. London, Spec. Publ.*, vol. 400, pp. 531–543, 2014, doi: 10.1144/SP400.15.

[11] G. Volckaert, L. Ortiz, P. De Canniere, M. Put, S. T. Horseman, J. F. Harrington, V. Fioravante, and M. Impey, "Modelling and experiments on gas migration in repository host rocks," *EUR 16235 MEGAS Final Rep. Phase 1*, p. 447, 1995.

[12] E. Jacops, G. Volckaert, N. Maes, E. Weetjens, and J. Govaerts, "Determination of gas diffusion coefficients in saturated porous media: He and CH4 diffusion in Boom Clay," *Appl. Clay Sci.*, vol. 83–84, pp. 217–223, 2013, doi: 10.1016/j.clay.2013.08.047.

[13] E. Jacops, K. Wouters, G. Volckaert, H. Moors, N. Maes, C. Bruggeman, R. Swennen, and R. Littke, "Measuring the effective diffusion coefficient of dissolved hydrogen in saturated Boom Clay," *Appl. Geochemistry*, vol. 61, pp. 175–184, 2015 doi: 10.1016/j.apgeochem.2015.05.022.

[14] D. Arnedo, E. Alonso, and S. Olivella, "Gas flow in anisotropic claystone: modelling triaxial experiments," *Int. J. Numer. Anal. Methods Geomech.*, vol. 37, pp. 2239–2256, 2013, doi: 10.1002/nag.2132.

[15] D. Arnedo, E. E. Alonso, S. Olivella, and E. Romero, "Gas injection tests on sand/bentonite mixtures in the laboratory. Experimental results and numerical modelling," *Phys. Chem. Earth*, vol. 33, pp. 237–247, 2008, doi: 10.1016/j.pce.2008.10.061.

[16] S. Olivella, a. Gens, J. Carrera, and E. E. Alonso, "Numerical formulation for a simulator (CODE_BRIGHT) for the coupled analysis of saline media," *Eng. Comput.*, vol. 13, no. 7, pp. 87–112, 1996, doi: 10.1108/02644409610151575.

[17] S. Olivella and E. E. Alonso, "Gas flow through clay barriers," *Géotechnique*, vol. 58, no. 3, pp. 157–176, 2008, doi: 10.1680/geot.2008.58.3.157.

[18] P. Delage, E. Romero, and A. Tarantino, "Recent developments in the techniques of controlling and measuring suction in unsaturated soils," in *Keynote Lecture, Proc. 1st Eur. Conf. on Unsaturated Soils, Durham, United Kingdom, July 2-4*, 2008, pp. 33–52.

[19] L. Q. Dao, Y. J. Cui, A. M. Tang, J. M. Pereira, X. L. Li, and X. Sillen, "Investigating the anisotropy of the shear modulus of natural Boom Clay," *Géotechnique Lett.*, vol. 4, pp. 98–101, 2014, doi: 10.1680/geolett.14.00015.

[20] A. Lima, "Thermo-Hydro-Mechanical Behaviour of two deep Belgian clay Formations: Boom and Ypresian clays," PhD thesis, Universitat Politècnica de Catalunya, Barcelona, Spain, 2011.

[21] E. Romero and P. H. Simms, "Microstructure investigation in unsaturated soils: A review with special attention to contribution of mercury intrusion porosimetry and environmental scanning electron microscopy," in *Laboratory and Field Testing of Unsaturated Soils*, Springer,., vol. 26, the Netherlands, 2009, pp. 93–115, doi: 10.1007/s10706-008-9204-5.

[22] F. Bernier, W. Bastiaens, and X. L. Li, "Twenty-five years' geotechnical observation and testing in the Tertiary Boom Clay formation," *Géotechnique*, vol. 57, no. 2, pp. 229–237, 2007, doi: 10.1680/geot.2007.57.2.229.

[23] M. De Craen, L. Wang, M. Van Geet, and H. Moors, "Geochemistry of Boom Clay pore water at the Mol site," *Sci. Rep. SCK·CEN-BLG-990*, 2004.

690 [24] L. Q. Dao, "Etude du comportement anisotrope de l'argile de Boom," PhD.
691 thesis, Université Paris-Est, Paris, France, 2015.

692 [25] X. Li, F. Bernier, T. Vietor, and P. Lebon, "Thermal impact on the damaged zone
693 around a radioactive waste disposal in clay host rocks. Deliverable 2.,"
694 *TIMODAZ, FI6W-CT-036449, Eur. Commision Proj.*, 2007.

695 [26] S. Yamamoto, M. Kumagai, K. Koga, and S. Sato, "Mechanical Stability of
696 Engineered Barriers in Sub-surface Disposal Facility during Gas Migration Based
697 on Coupled Hydro-Mechanical Modelling," *Geol. Soc. London, Spec. Publ.*, vol.
698 415, pp. 213–224, 2015, doi: 10.1144/SP415.11.

699 [27] M. Fall, O. Nasir, and T. S. Nguyen, "A coupled hydro-mechanical model for
700 simulation of gas migration in host sedimentary rocks for nuclear waste
701 repositories," *Eng. Geol.*, vol. 176, pp. 24–44, 2014, doi:
702 10.1016/j.enggeo.2014.04.003.

703 [28] H. H. Liu, J. Rutqvist, and J. G. Berryman, "On the relationship between stress
704 and elastic strain for porous and fractured rock," *Int. J. Rock Mech. Min. Sci.*, vol.
705 46, pp. 289–296, 2009, doi: 10.1016/j.ijrmms.2008.04.005.

706 [29] H. H. Liu, J. Rutqvist, and J. T. Birkholzer, "Constitutive relationships for elastic
707 deformation of clay rock: Data analysis," *Rock Mech. Rock Eng.*, vol. 44, no. 4,
708 pp. 463–468, 2011, doi: 10.1007/s00603-010-0131-4.

709 [30] R. Senger, E. Romero, and P. Marschall, "Modeling of gas migration through
710 low-prermeability clay using information on pressure and deformation from fast
711 air injection tests," *PROCEEDINGS, TOUGH Symp. 2012 Lawrence Berkeley
712 Natl. Lab. Berkeley, California, Sept. 28-30, 2015*, pp. 1–5, 2015.

713 [31] P. Gerard, J. Harrington, R. Charlier, and F. Collin, "Modelling of localised gas
714 preferential pathways in claystone," *Int. J. Rock Mech. Min. Sci.*, vol. 67, pp.
715 104–114, 2014.

716 [32] E. E. Alonso, S. Olivella, and D. Arnedo, "Mechanisms of gas transport in clay
717 barriers," *J. Iber. Geol.*, vol. 32, no. 2, pp. 175–196, 2006.

718 [33] E. E. Alonso, A. Gens, and A. Josa, "A constitutive model for partially saturated
719 soils," *Géotechnique*, vol. 40, no. 3, pp. 405–430, 1990.

720

721 **TABLES:**

722 Table 1. Boom Clay properties and initial conditions.

Main properties / initial conditions	**Symbol**	**Value**
Density of solids	ρ_s	2.67 Mg/m^3
Liquid limit	w_L	67%
Plastic limit	w_P	29%
Dominant entrance pore size from MIP		70 nm
Air-entry value from dominant entrance pore size		4.8 MPa
Dry density	ρ_d	1.66-1.69 Mg/m^3
Void ratio	e	0.57-0.61
Water content	w	22.6-24.0%
Degree of saturation	S_r	close to 1
Total suction	ψ	2.5 MPa

723

724 Table 2. Parameters of the BBM model [33] used in the simulations.

Definition parameter	Symbol	Value
Elastic behaviour		
Elastic compressibility (against mean stress changes)	κ	0.020
Volumetric compressibility against suction changes	κ_s	0.005
Poisson ratio	v	0.33
Plastic and shear strength behaviour		
Elastoplastic volumetric compressibility	$\lambda(0)$	0.10
Parameters to define loading-collapse yield curve	r	0.95
	β	4 MPa^{-1}
Parameter to define increase in cohesion with suction	k	0.01
Reference stress	P_c	0.1 MPa
Slope of critical state line	M	0.73
Parameter for the plastic potential	α	0.333
Initial state		
Initial preconsolidation stress for saturated conditions	p_0^*	6 MPa
Lateral earth pressure at rest	K_0	0.84
Initial void ratio	e_0	0.57

725

726 Table 3. Hydraulic parameters used in the simulations.

Definition parameter	Symbol	Value
Kozeny´s model		
Reference intrinsic permeability	k_0	$4.2 \cdot 10^{-19}$ m^2
Reference porosity	ϕ_0	0.363
Embedded fracture permeability model		
Reference intrinsic permeability	k_0	$4.2 \cdot 10^{-19}$ m^2
Reference porosity	ϕ_0	0.363
Initial aperture	b_0	$1 \cdot 10^{-7}$ m
Threshold strain	ε_0	$-1 \cdot 10^{-4}$
Characteristic dimension	s	$3 \cdot 10^{-5}$ m
Retention curve (van Genuchten's model)		
Shape function for retention curve	λ	0.6
Material parameter related to air entry value	P	10 MPa
Residual saturation	S_{rl}	0.2
Maximum saturation	S_{ls}	1
Liquid relative permeability		
Power	n	1.48
Gas relative permeability		
Constant	A	1
Power	β	2.8
Diffusion of dissolved air		
Molecular diffusion coefficient	D_m^a	$5 \cdot 10^{-10}$ m^2/s

727

728 Table 4. Stages and pressure boundary conditions for the simulation of slower air
729 injection test.

Time (min)	Stage	Boundary conditions
0-500	Replace water by air	Upstream air pressure increases up to 0.5 MPa Downstream pressure constant (0.5MPa)
500-745	Air injection (r=2 mL/min)	Upstream pressure increases from 0.5 to 4 MPa Downstream pressure constant (0.5MPa)
745-1080	Air dissipation	Upstream boundary becomes impermeable Downstream pressure constant (0.5MPa)
1080-2300	Air dissipation	Upstream boundary remains impermeable Downstream pressure increases up to 1.5 MPa

730

731 Table 5. Stages and pressure boundary conditions for the simulation of faster air
732 injection test.

Time (min)	Stage	Boundary conditions
0-500	Replace water by air	Upstream air pressure increases up to 0.5 MPa Downstream pressure constant (0.5MPa)
500-504.87	Air injection (r=100 mL/min)	Upstream pressure increases from 0.5 to 4 MPa Downstream pressure constant (0.5MPa)
504.87-535.68	Air dissipation	Upstream boundary becomes impermeable Downstream pressure constant (0.5MPa)
535.68-541.68	Air dissipation	Upstream boundary remains impermeable Downstream pressure increases up to 1.8 MPa
541.68-2000	Air dissipation	Upstream boundary remains impermeable Downstream pressure constant (1.8 MPa)

733

734 **FIGURES:**

735 Figure 1. Drying branch of the water retention curve of intact Boom Clay.

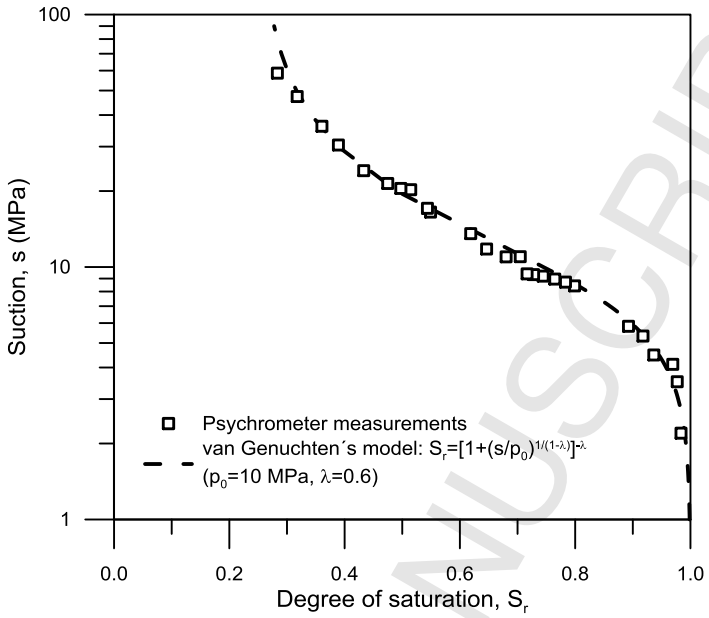

736

737

738 Figure 2. Pore size density function of intact Boom Clay samples.

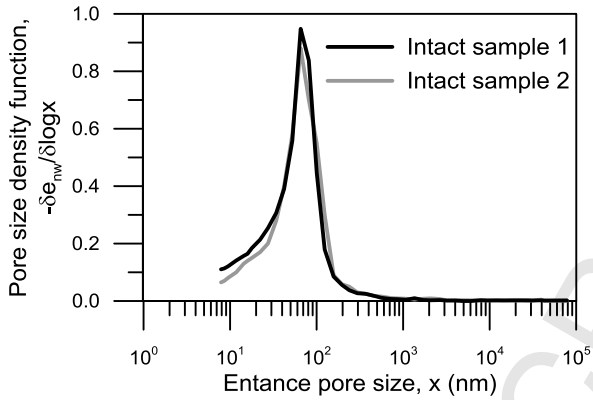

739

740

741 Figure 3. Scheme and picture of the experimental set-up. 1) Oedometer cell; 2) sample;
742 3) coarse porous concentric rings; 4) axial loading piston; 5) pressure/volume controller
743 for vertical stress; 6) air pressure/volume controller; 7) and 8) water pressure/volume
744 controllers; 9) LVDT; 10) acquisition system.

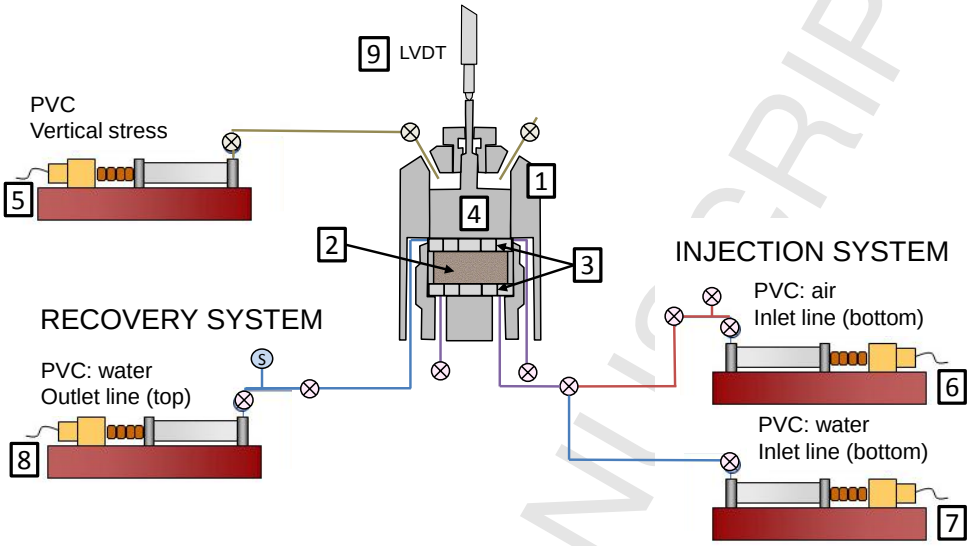

745

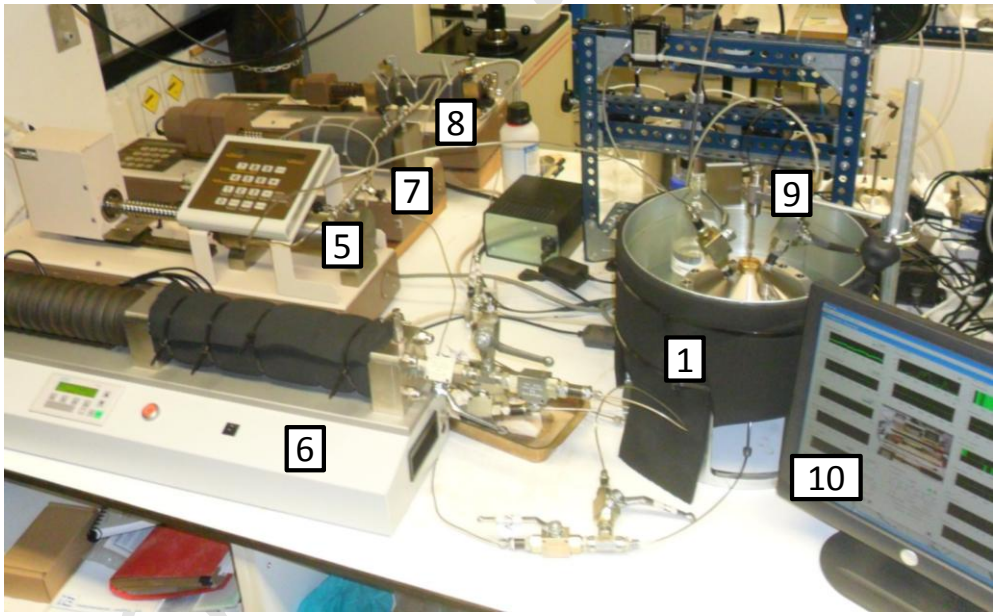

746

747

748 Figure 4. Scheme of test protocols followed: 1) Pre-conditioning path: a) undrained
749 loading; b) contact with SBCW. 2) Water permeability determination. 3) Drained
750 loading. 4) Fast replacement of water by air at the bottom cap. 5) Air injection and
751 dissipation stages. 6) Undrained unloading.

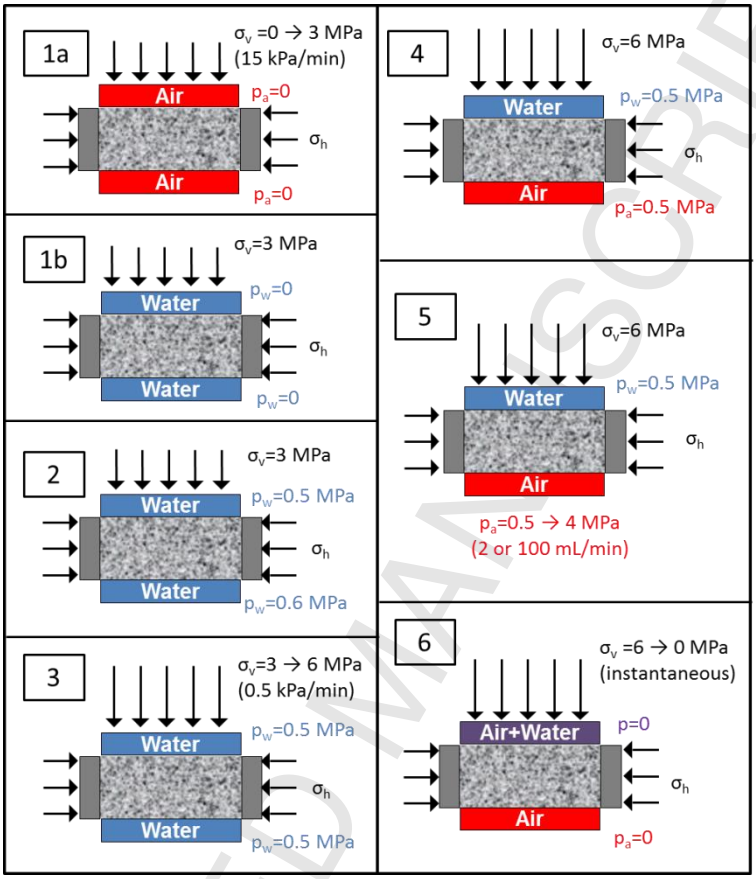

752
753

754 Figure 5. Compressibility curves including water undrained loading to in situ
755 conditions, contact with SBCW, and drained loading and unloading.

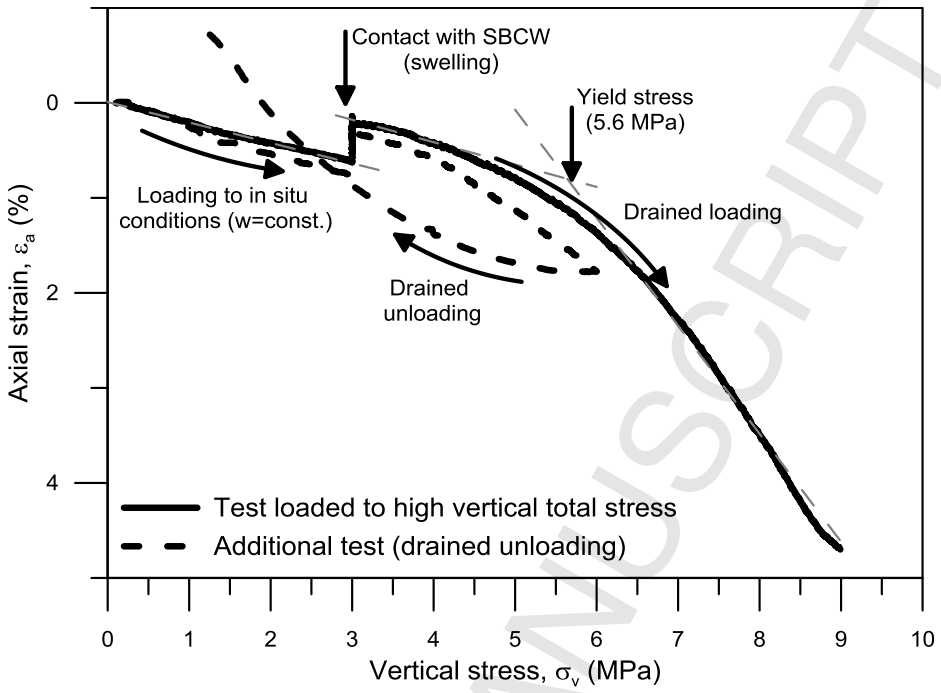

756

757

758 Figure 6. Water permeability as a function of the average void ratio for samples
759 orientated with bedding planes parallel to flow.

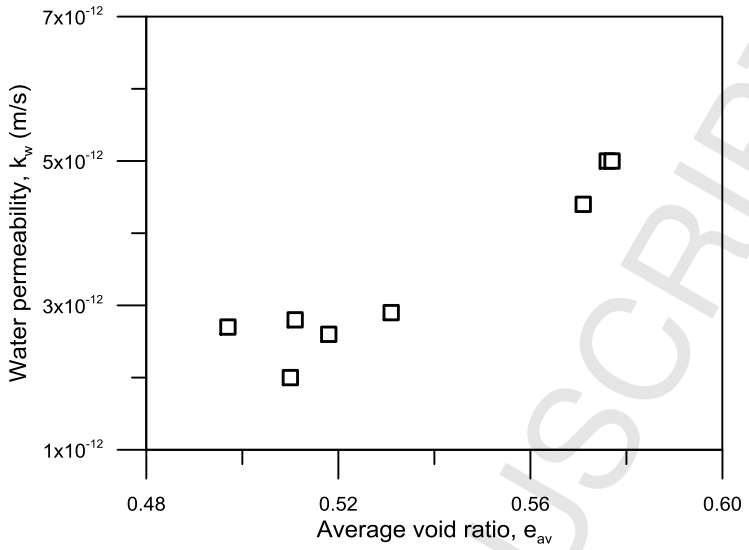

760

761

762 Figure 7. Time evolution of outflow volume, axial strain, and pressures at the injection
763 (inflow) and recovery (outflow) boundaries, for the two injection rates. A to B: air
764 injection stage; B: shut-off; B to C: dissipation stage.

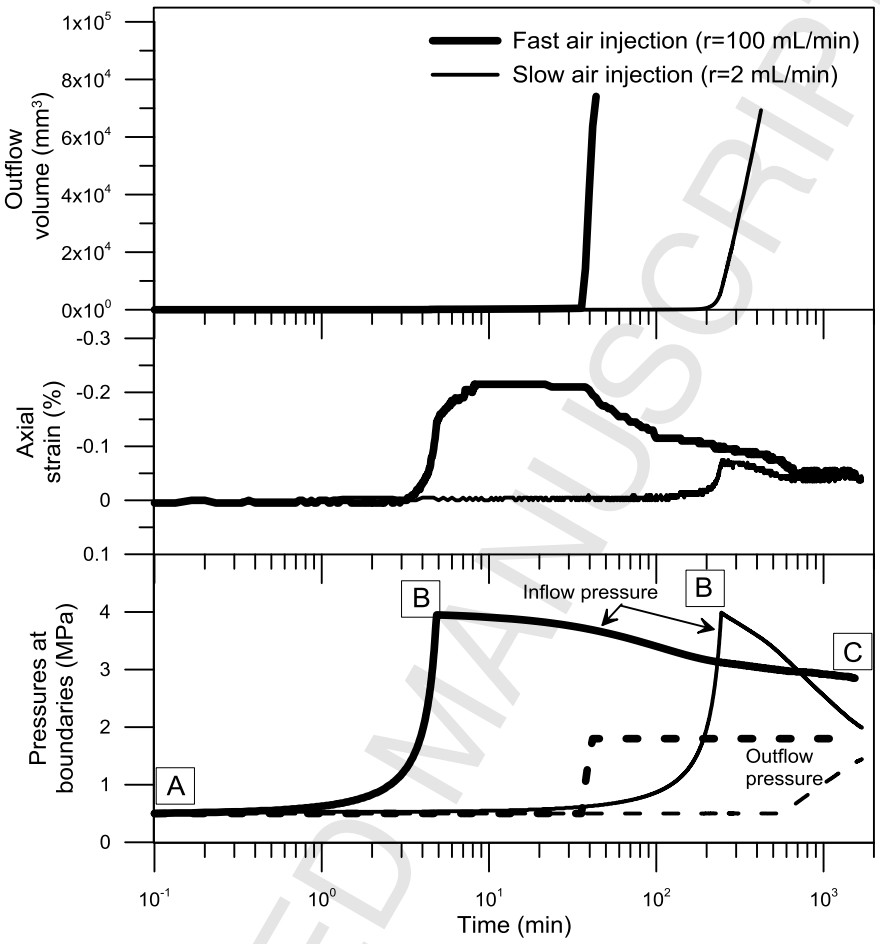

765

766

767 Figure 8. Axial strains against constitutive stress (vertical stress minus air pressure at
768 the upstream boundary) for tests at two injections rates.

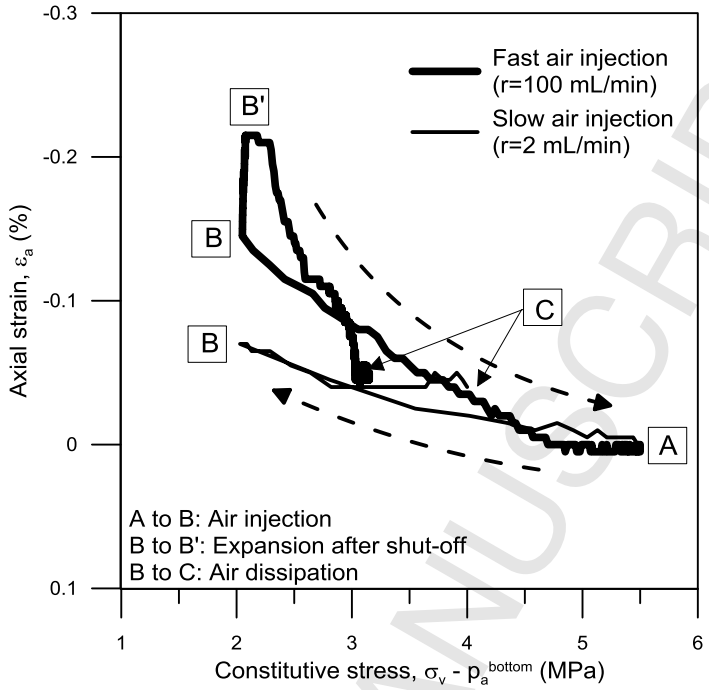

769

770

771 Figure 9. Drained constrained stiffness during the unloading paths and during the air
772 injection stages under oedometer conditions.

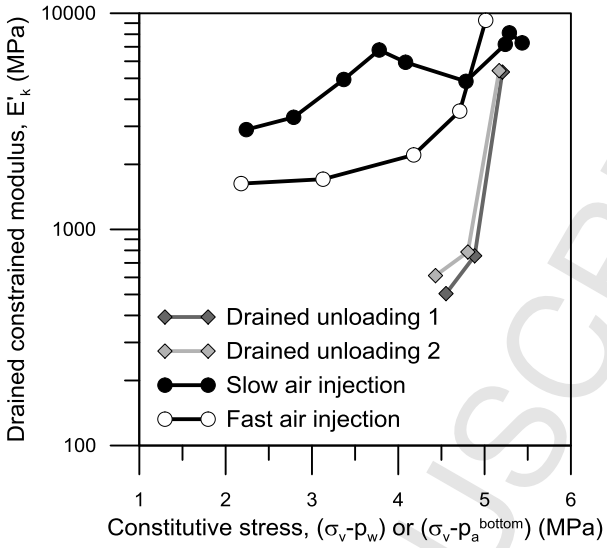

773

774

775 Figure 10. Pore size distribution changes before and after air injection tests.

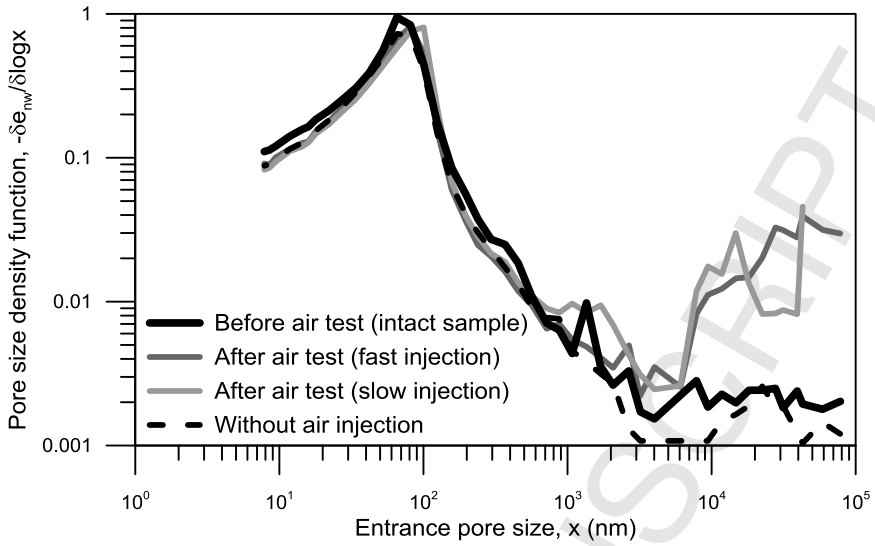

776

777

778 Figure 11. Fractal analysis of the pore network before and after air injection tests.

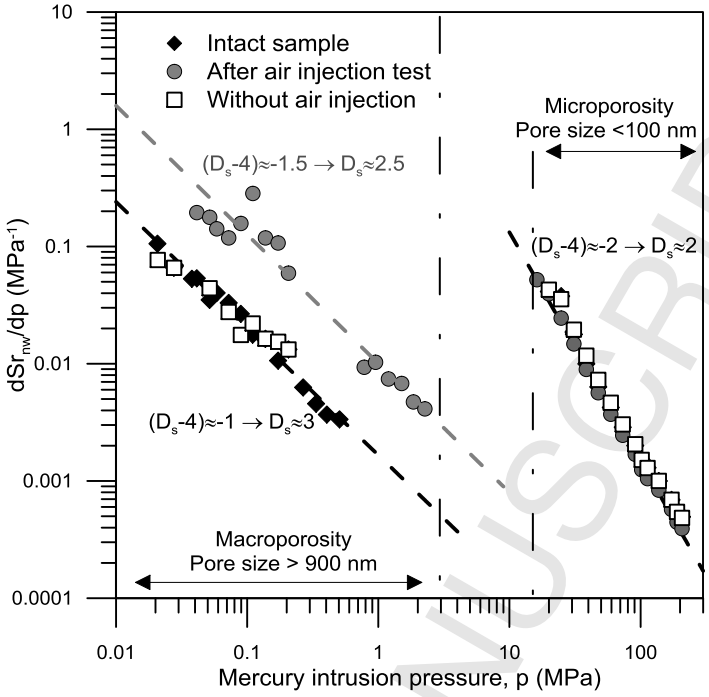

779

780

781 Figure 12. Computed versus measured axial strains during hydro-mechanical loading.

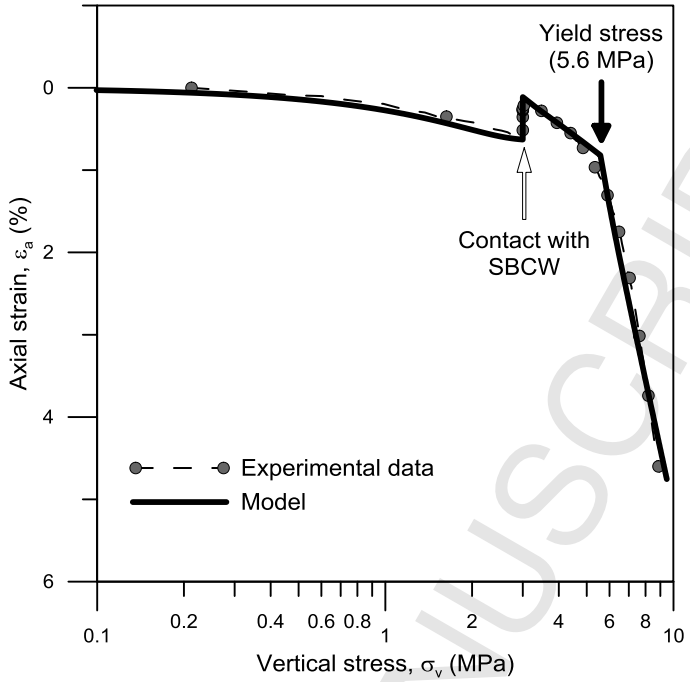

782

783

784 Figure 13. Intrinsic permeability changes with void ratio together with fitted Kozeny's
785 model.

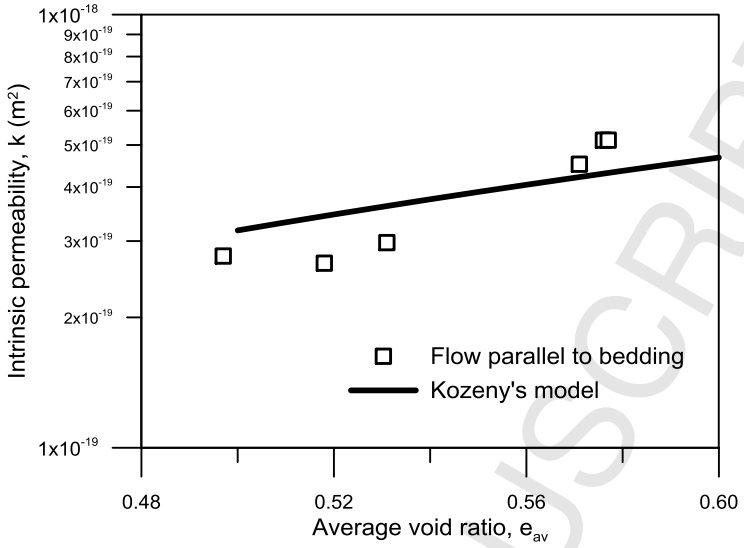

786

787

788 Figure 14. Theoretical variation of intrinsic permeability and capillary pressure in the
789 fracture. Initial and final values for the set of parameters indicated in Table 3.

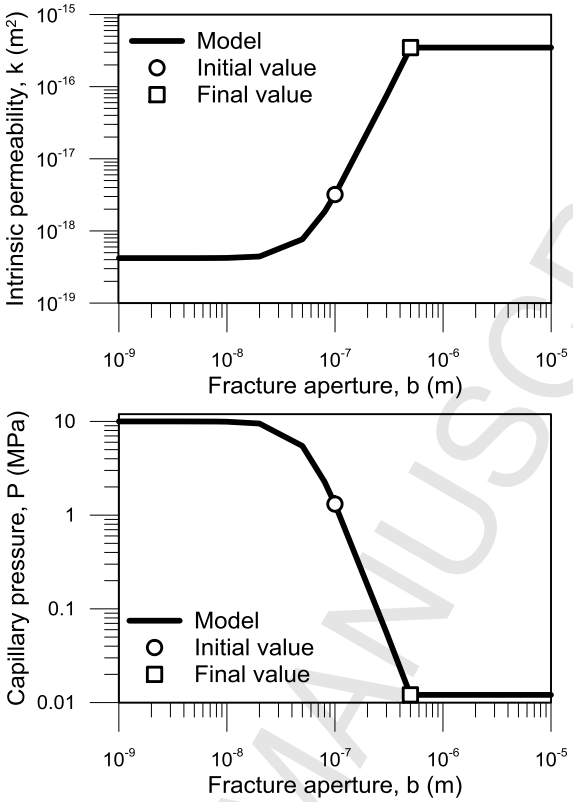

790

791

792 Figure 15. Experimental water retention curves before (matrix) and after (fracture) air
793 tests together with their modelling curves.

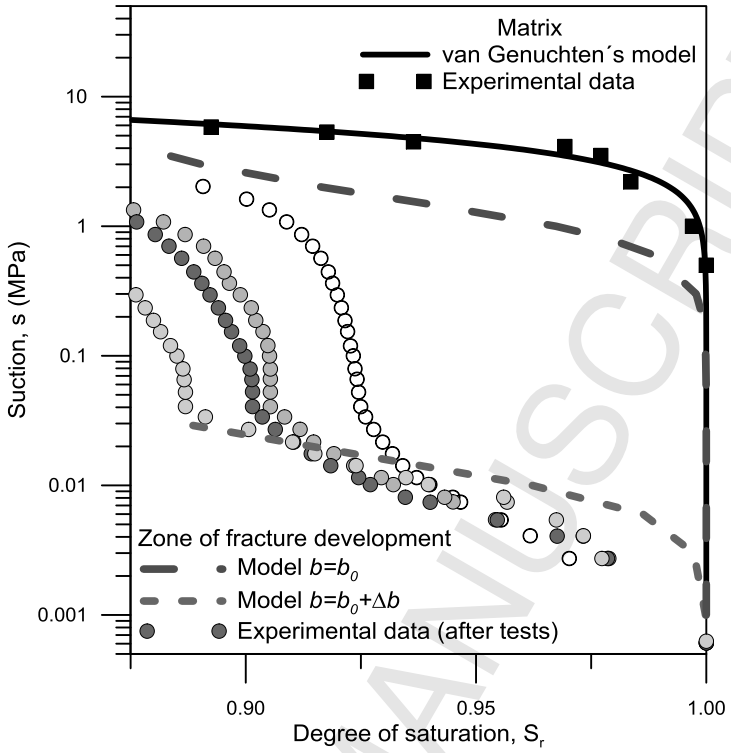

794

795

796 Figure 16. Materials and geometry for numerical simulation.

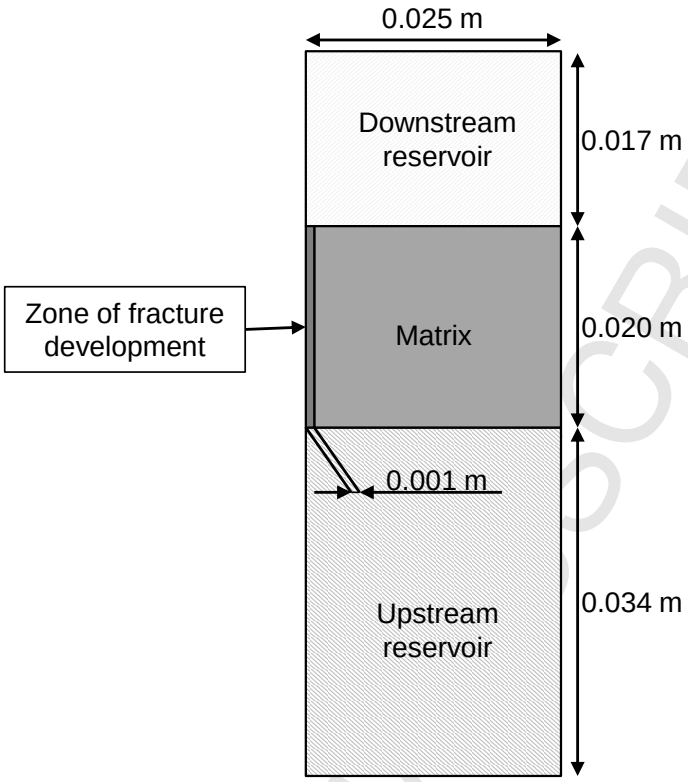

797

798

799 Figure 17. Computed versus measured in the ZFD (at 0.0005 mm from the axis): a)
800 injection and recovery pressures; b) average axial strains; c) outflow volumes. Slower
801 air injection test.

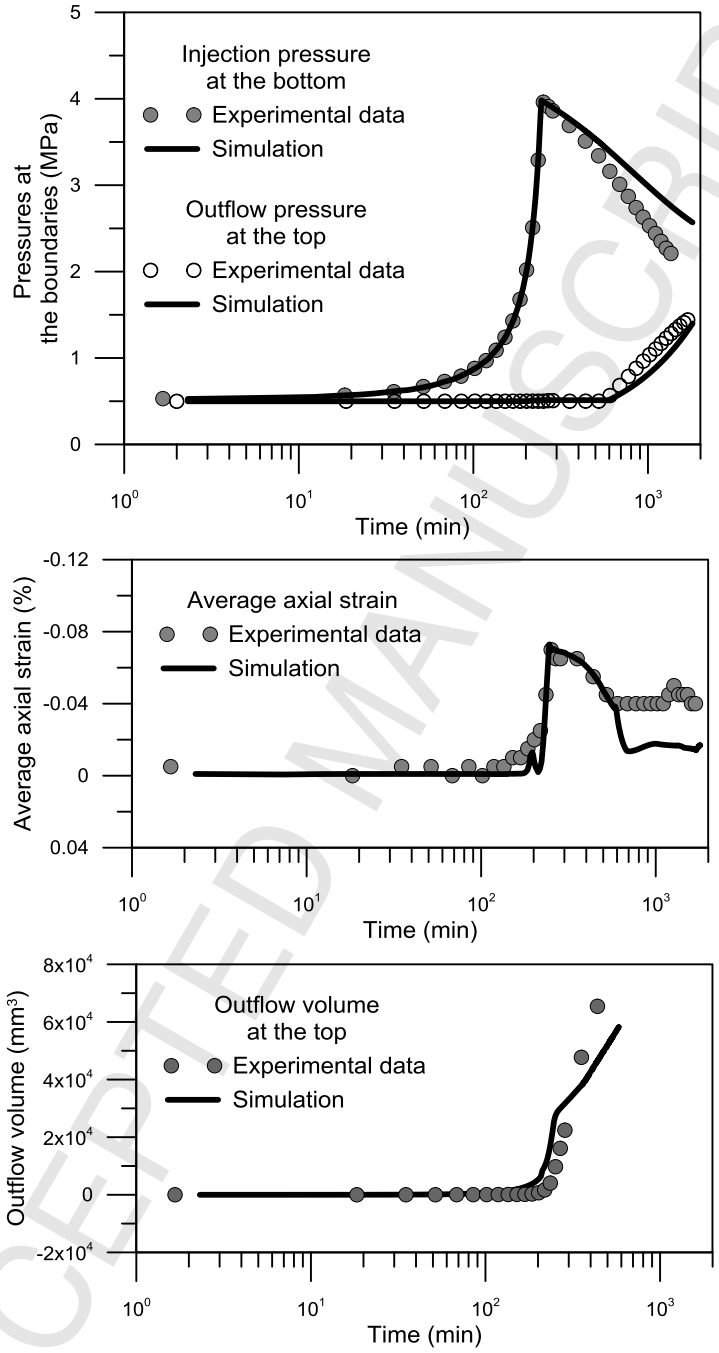

802

803

Figure 18. Simulated distribution of absolute gas pressure (left, in MPa), porosity (middle) and liquid degree of saturation (right) during the air injection (t=150 min), at shut-off (t=245 min) and during the dissipation (t=600 min).

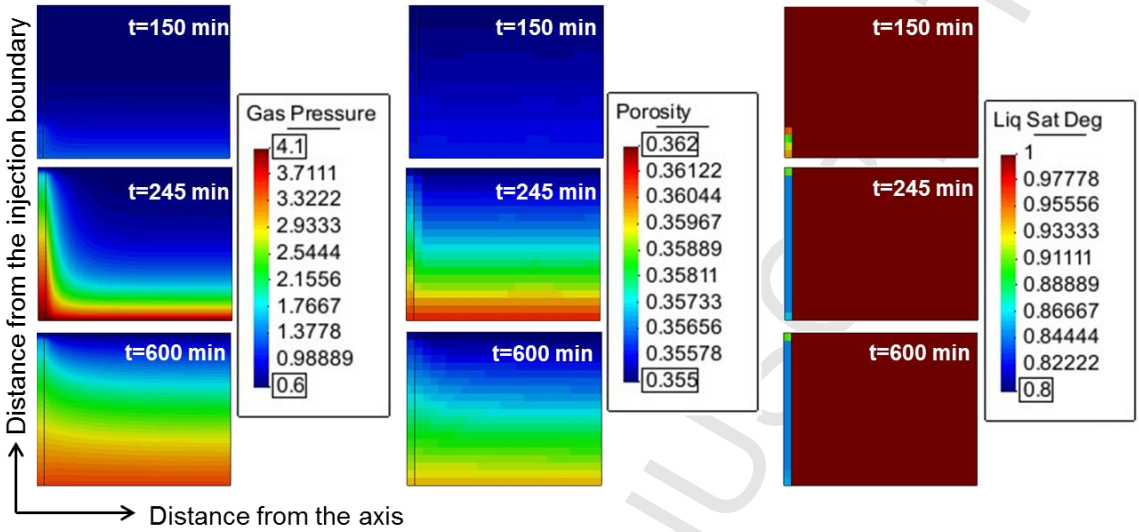

809 Figure 19. Diffusive and advective fluxes along the core height in the ZFD (at 0.0005
810 mm from the axis) and in the matrix (at 0.0125 mm from the axis) at air injection (t=150
811 min), shut-off (t=245 min) and dissipation (t=600 min) stages.

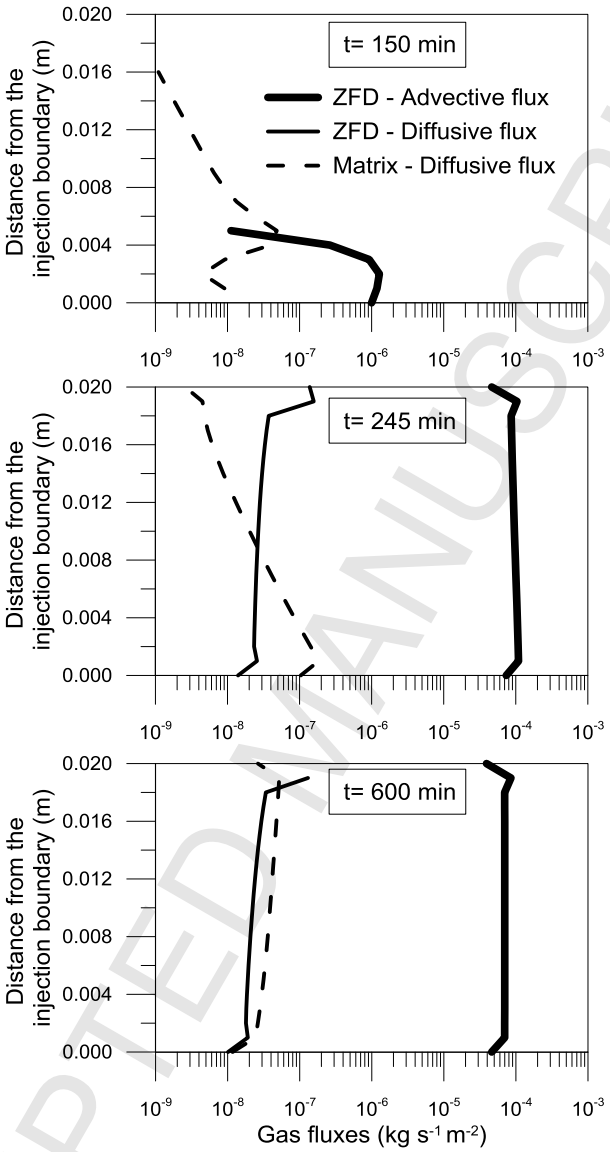

812

813

814 Figure 20. Simulated vertical profiles of gas pressure, P_g, and liquid pressure, P_l,
815 throughout the core height in the ZFD (at 0.0005 mm from the axis) at air injection
816 (t=150 min), shut-off (t=245 min) and dissipation (t=600 min) stages.

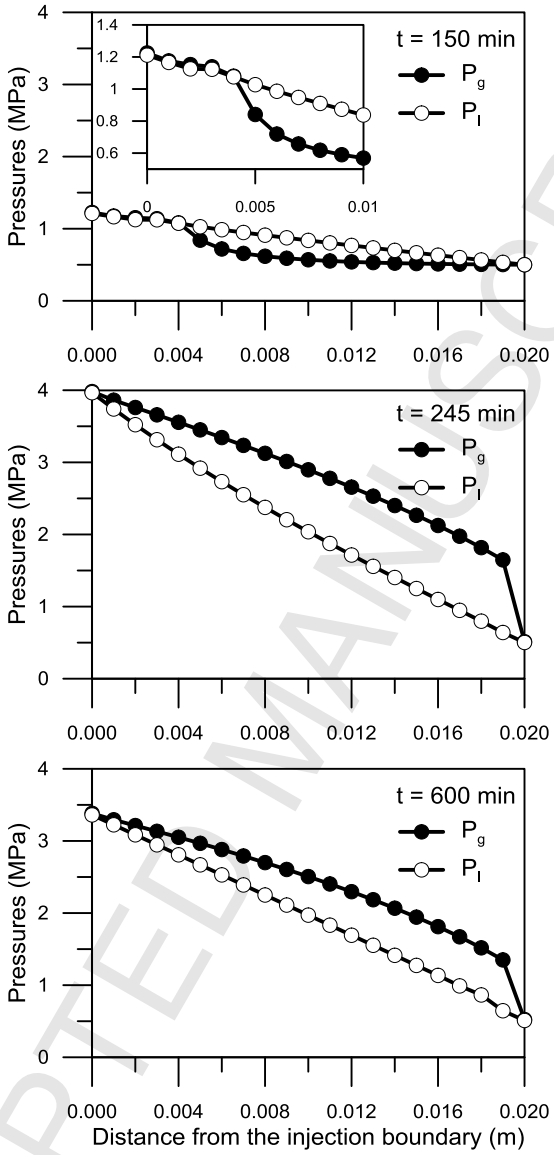

817

818

819 Figure 21. Computed local radial strains and radial displacements at the mid-height of
820 the sample as a function of the distance from the symmetry axis at air injection (t=150
821 min), shut-off (t=245 min) and dissipation (t=600 min) stages.

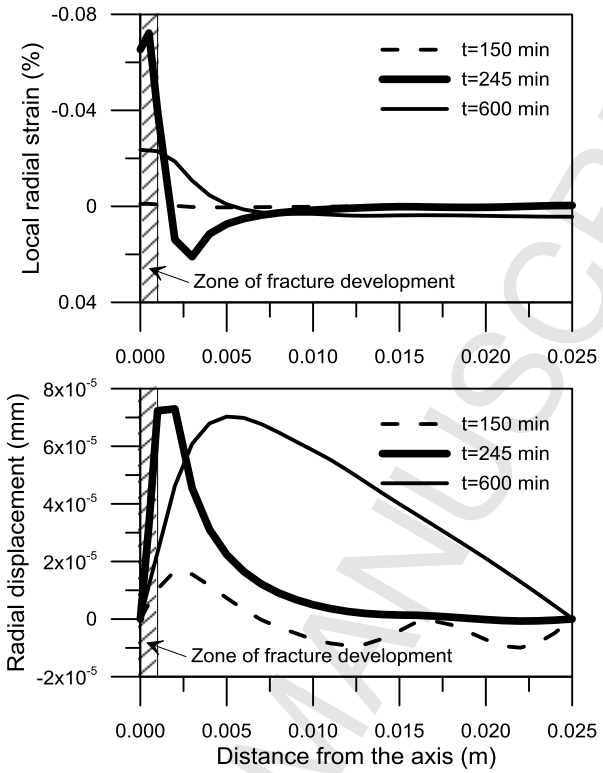

822

823

824 Figure 22. Computed versus measured in the ZFD (at 0.0005 mm from the axis): a)
825 injection and recovery pressures; b) axial strains; c) outflow volumes. Faster air
826 injection test.

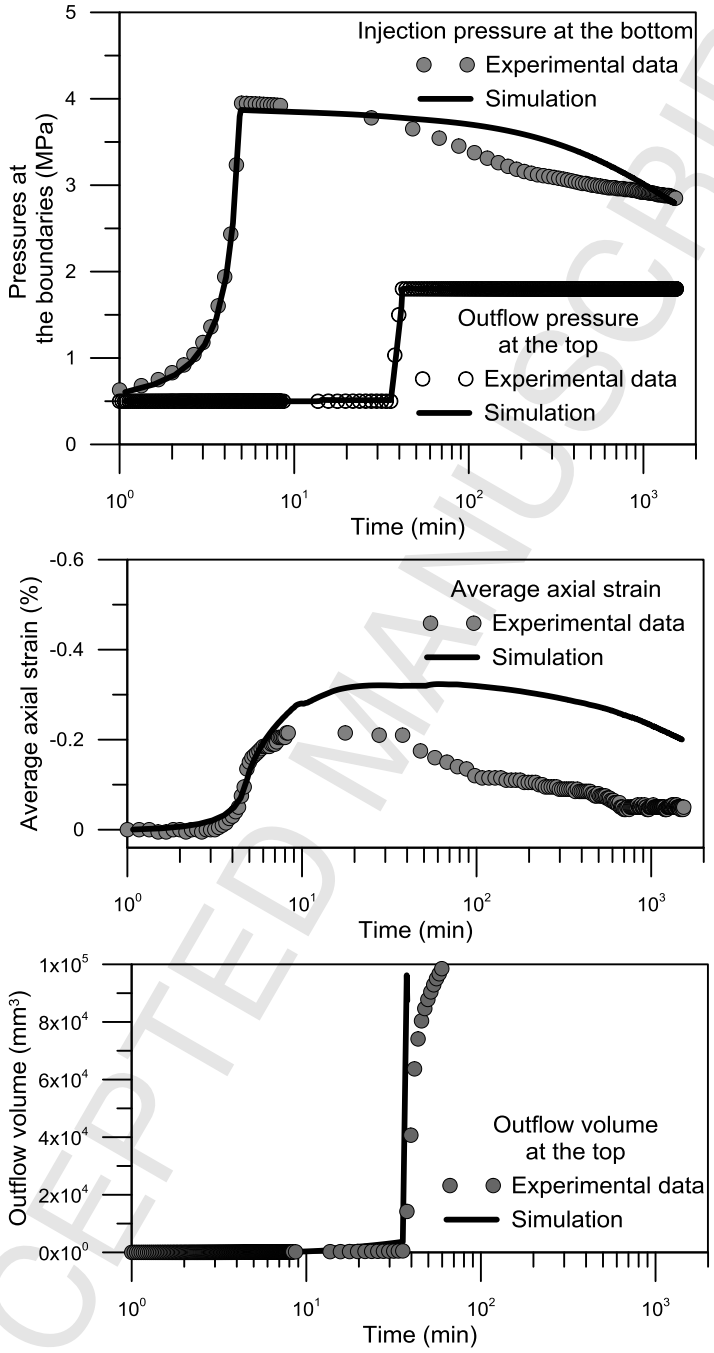

827

Highlights:

- Volume changes due to gas injection and pressure release are measured
- Opening of preferential paths can occur even in a constrained setup (local strains)
- Gas transport rate depends on volumetric strains and preferential path opening
- Opening of fractures after gas injection is confirmed by MIP tests
- Aperture changes affected the intrinsic permeability and air-entry value